Langmuir, 2019, published 08/05/2019; DOI: 10.1021/acs.langmuir.9b01748

Phase Behavior and Capillary Condensation Hysteresis of Carbon Dioxide in Mesopores

Silvio Dantas[1], *Katie Cychosz Struckhoff*[2], *Matthias Thommes*[3*], *Alexander V. Neimark*[1*]

1. Department of Chemical and Biochemical Engineering, Rutgers, The State University of New Jersey, 98 Brett Road, Piscataway, New Jersey 08854, United States

2. Anton Paar Quantatec Inc., 1900 Corporate Dr, Boynton Beach, Florida 33426, United States

3. Department of Chemical and Bioengineering, Institute of Separation Science and Technology, Friedrich-Alexander University Erlangen-Nürnberg, 91058, Erlangen, Germany

* email for correspondence: aneimark@rutgers.edu, matthias.thommes@fau.de

Abstract

Carbon dioxide adsorption on micro- and mesoporous carbonaceous materials in a wide range of temperatures and pressures is of great importance for the problems of gas separations, greenhouse gas capture and sequestration, enhanced hydrocarbon recovery from shales and coals, as well as for the characterization of nanoporous materials using CO_2 as a molecular probe. We investigate

the influence of temperature on CO_2 adsorption focusing on the capillary condensation and hysteresis phenomena. We present experimental data on adsorption of CO_2 on CMK-3, ordered carbon with mesopores of ~5-6 nm, at various temperatures (185 K – 273 K) and pressures (up to 35 bars). Using Monte Carlo simulations in the grand canonical and mesocanonical ensembles, we attempt to predict the transition from reversible capillary condensation to hysteric adsorption-desorption cycles that is experimentally observed with the decrease of temperature. We show that, while the desorption at all temperatures occurs at the conditions of pore vapor-liquid equilibrium, the capillary condensation is a nucleation-driven process associated with a particular energy barrier of ~43 kT, specific to the sample used in this work. This barrier can be overcome at the equilibrium conditions in the region of reversible condensation at temperatures higher 240 K. At lower temperatures, the regime of developing hysteresis is observed with the progressively widening hysteresis loop. The position of capillary condensation transition is estimated using the pressure dependence of the energy barrier calculated by thermodynamic integration of the van-der-Waals type continuous canonical isotherm simulated with the gauge cell MC method. These findings lay the foundation for developing kernels of CO_2 adsorption and desorption isotherm for calculating pore size distribution in the entire range of micropore and mesopore sizes from the one high pressure experimental isotherm.

Introduction

Specifics of CO_2 adsorption on nanoporous materials, especially, on micro- and mesoporous carbons, have been attracting continuous interest of interdisciplinary scientific communities due to pressing problems of CO_2 separation, capture, and sequestration, as well as the use of CO_2 in enhanced gas recovery from shales and coal.[1-2] Carbon dioxide has proven to be a suitable probe molecule to characterize microporous carbons due to its ability to be adsorbed at ambient

temperatures, allowing for faster diffusion rates and penetration into narrowest micropores not normally accessible by cryogenic adsorbates.[3-4] Recent technological advances in adsorption instrumentation technology have enabled reliable gas adsorption experiments performed with automated adsorption instruments using carbon dioxide at high pressures and temperatures.[5] As a result, the appraisal of the pore size distributions over the full micro- and mesopore range from one experimental CO_2 isotherm becomes available. Quantitative interpretation of measured isotherms requires a better understanding of the CO_2 adsorption and phase behavior in micro- and mesopores, most importantly, of the mechanisms of capillary condensation and hysteresis. The main challenge resides in predicting the pressure of condensation in so-called regime of developing hysteresis[6] as a function of the pore size and temperature. Here, we report experimental adsorption data of CO_2 on ordered mesoporous carbons of CMK-3 type over the wide ranges of temperatures (from 273 K down to 185 K) and pressure up to the saturation (~35 bar at 273 K). The experimental observations are explained using the Monte Carlo (MC) simulations harnessed with the theoretical analysis of the nucleation phenomena during capillary condensation.

The use of carbon dioxide as a probe molecule for adsorption measurements was proposed at temperatures close to 273 K [7], as a way to overcome critical limitations observed with traditionally used cryogenic adsorbates (e.g. N_2 – 77 K and Ar – 87 K). Due to nitrogen's quadrupole moment and strong interactions with carbon surfaces, diffusion into smaller pores is effectively inhibited. Argon facilitates the resolution of smaller micropores (~ 0.5 nm) at higher relative pressures than N_2.[7-8] However, activated carbons may contain significant amounts of ultra-micropores (< 0.5 nm) and access to these micropores is further limited by diffusion. Carbon dioxide, with slightly smaller kinetic diameter and high temperature of adsorption, enables higher diffusion rates, ultimately producing better resolution of ultra-micropores.[9] With access to a wide range of relative pressures,

from ultra-high vacuum ($P/P_0 = 10^{-7}$) to pressures up to more than 200 bar, one can measure full subcritical CO_2 adsorption isotherms. The application of modern methods based on MC and density functional theory (DFT) simulations for interpretation of adsorption measurements allows for an accurate evaluation of the pore size distributions of nanoporous materials, including ordered mesoporous carbons within the whole micro- and mesopore range.

With high microporosity, carbon-based materials are widely used for many applications including capture and sequestration of gases[10], filtration processes[11], energy storage[12], catalysis[13]. In the search for new structures, advanced templating procedures have been developed leading to the synthesis of ordered mesoporous carbon materials[14]. In 2000, Ryoo and co-workers[15] reported the synthesis the first CMK-3, an ordered nanoporous carbon material that retains the same structural symmetry as its template, SBA-15[16], a well-known ordered mesoporous silica molecular sieve. The ability to tune the width of the primary group of pores on such well-ordered structures enables the synthesis of materials with large pore surface area and pore volume. Comprehensive understanding the textural properties (e.g. surface area, pore size, porosity) of these materials is key to perfecting their use in catalysis, separations, and many other applications[8]. With most of the pores in CMK-3 carbons being in the mesopore range, a better understanding of the process of capillary condensation and the possible hysteresis behavior that can be observed under certain conditions are required.

Capillary condensation represents a phenomenon of gas condensation in pores to a liquid-like phase at a pressure smaller than the saturation pressure, P_0, of the bulk fluid. Due to the influence of pore confinement, the vapor-liquid transition occurs below the pore critical temperature, T_{cp}, which is smaller than the bulk critical temperature.[17] Provided the pores are sufficiently large, capillary condensation is accompanied by hysteresis. In the absence of pore network effects,

hysteresis in cylindrical pore channels is solely determined by the effect of delayed condensation (due to metastable pore fluid), while the desorption branch reflects the liquid-vapor equilibrium transition.[18] The hysteresis phenomenon depends on temperature and pore size: increase in temperature has a qualitatively similar effect as decrease in the pore size, leading to reduction in the width of the hysteresis loop. For given pore size, the hysteresis loop eventually disappears at a so-called hysteresis critical temperature T_h, which is below T_{cp}.[6, 19] For given temperature, the positions of phase transformations depend on the pore size, and the hysteresis appears in pores wider than a certain hysteresis critical pore size. From the comparison of the canonical ensemble van-der-Waals type isotherms generated by the mesocanonical ensemble gauge cell MC simulation and classical DFT simulations with the experiments, the authors[6] have classified the adsorption isotherms into four regimes. (1) supercritical sorption without phase separation above the pore critical temperature, $T > T_{cp}$; (2) reversible capillary condensation between the pore critical temperature and the hysteresis critical temperature, $T_h < T < T_{cp}$; (3) irreversible capillary condensation with developing hysteresis loop as temperature reduces below the hysteresis critical temperature, $T < T_h$; and (4) irreversible capillary condensation with developed hysteresis loop. A hysteresis loop is considered *developed*, when capillary condensation occurs at the limit of metastability of the vapor-like state (vapor-like spinodal), and *developing*, if capillary condensation occurs between the equilibrium and the vapor-like spinodal. Similar regimes are observed for the isotherms at fixed temperature and varying pore size. It is worth noting that the nucleation-driven phase transitions depend on temperature, pore size and fluid-solid pair.[20]

The use of molecular simulations can be invaluable to the characterization of materials such as CMK-3 materials, as they can exhibit all of the capillary condensation regimes described earlier. Under subcritical conditions, grand canonical Monte Carlo (GCMC)[21] simulations allow for

calculations of the adsorption and desorption branches that form the hysteresis loop, which represent the spontaneous condensation and evaporation of the system. Amongst several methods that have been developed[22-25] to determine the equilibrium transition between states under confinement, the gauge cell method[26-27] has been proven to be useful and reliable.[28-36] Mesocanonical ensemble gauge cell MC method allows for calculating the equilibrium transition and the spinodal limits of stability of the vaporlike and liquidlike metastable states, and furthermore, for estimating the energy barriers that separates them. The key aspect of this method is the use of a gauge cell set in chemical and thermal equilibrium with the system cell that contain the adsorbent that allows for calculating the chemical potential of the adsorbed phase and constructing the continuous van-der-Waals type adsorption isotherm.[26-27] Of special interest is the recent work[31], where the gauge cell simulations were used to calculate the nucleation barriers for capillary condensation of Ar and analyze the different capillary condensations regimes observed experimentally at three temperatures and for two different MCM-41 samples.

In the present study, we explore the phase behavior of CO_2 under the confinement of micro-mesoporous carbon nanoporous materials at various temperatures through high pressure CO_2 adsorption experiments and MC simulations in the grand canonical and mesocanonical ensembles. Experimental adsorption data at 185-273 K is obtained on a CMK-3 sample with micropores of about 1 nm and mesopores of about 6 nm. As the temperature decreases, a gradual transition is observed from reversible to hysteretic isotherms, and below the triple point, to reversible isotherms limited by desublimation. Theoretical isotherms are obtained at 210, 220, 240 and 273 K using the TraPPE model[37] for CO_2 and a Lennard-Jones (LJ) solid-fluid potential to implicitly represent the carbon pore walls of 6 nm in diameter. Using both grand canonical and mesocanonical ensembles, we accurately identify the positions of equilibrium vapor-liquid transition and of the vapor and

liquid transitions that correspond to the limit of stability of respective vapor-like and liquid-like phases. To properly predict capillary condensation, we calculate the pressure dependence of the nucleation barrier for condensation. From the comparison between experiments and simulations, we estimate a characteristic energy barrier of ~43 kT, which represents the critical barrier that has to be overcome to transit from vapor to condensed states. This finding allows us to predict the experimentally observed features of CO_2 capillary condensation and reproduce the adsorption isotherms in the regime of developing hysteresis.

Methodology

Experimental measurements - *High Pressure CO_2 adsorption*

Ordered mesoporous carbon samples[38-39] were outgassed at 423 K for 12 h under turbomolecular pump vacuum. Ar (87 K) and N_2 (77 K) adsorption measurements were performed on a high-resolution low pressure nanometric adsorption equipment (Quantachrome Instruments Autosorb-iQ MP). CO_2 high pressure adsorption measurements were executed on a Quantachrome Instruments iSorb HP. Temperatures below 263 K were maintained by using Quantachrome Instruments' CryoCooler.

Molecular modeling

The modelled pore structure for the carbon adsorbent is composed of perfectly smooth, rigid, and infinitely long cylindrical pores. The simulations are performed in a cubic cell with periodic boundary conditions on all three axes with "padding" of half of the cutoff distance added to the sides of the pore. Carbon dioxide is modelled by using the TraPPE model[37] with 15 Å cutoff, Ewald summation, and tail corrections, in order to reproduce bulk properties properly in the range of temperatures of interest (see Supporting Information, Section A). All simulations were performed using the MCCCS Towhee software package[40] with the addition of the cylindrical solid-

fluid potential, equation 1 [41]. In equation 1, r is the distance between the fluid atom and the center of the cylinder; R represents half of the diameter of the cylindrical potential, that differs from the internal pore diameter by $\sigma_s = 0.34\ nm$; ρ_A is the area density of carbons atoms in the pore surface; $\sigma_{sf}\ and\ \epsilon_{sf}$ are the LJ solid-fluid interaction parameters; F(a,b,c,d) is the hypergeometric function. The Lennard Jones (LJ) parameters employed are as follows: $\sigma_{O-O} = 0.305\ nm$, $\epsilon_{O-O}/k_b = 79\ K$, $\sigma_{s-O} = 0.3225\ nm$, $\epsilon_{s-O}/k_b = 46.184\ K$, $\sigma_{C-C} = 0.28\ nm$, $\epsilon_{C-C}/k_b = 27\ K$, $\sigma_{s-C} = 0.31\ nm$, and $\epsilon_{s-C}/k_b = 27\ K$ with $\rho_A = 38.19\ nm^{-2}$. The solid-fluid interaction parameters, ϵ_{sf} and σ_{sf}, are calculated using Lorentz-Berthelot mixing rules with the fluid-fluid TraPPE parameters and solid-solid parameters, $\sigma_{s-s} = 0.34\ nm$, and $\epsilon_{s-s}/k_b = 27\ K$, determined from fitting to the experimental data.[42]

$$U_{sf}(r) = \pi^2 \rho_A {\sigma_{sf}}^2 \epsilon_{sf} \left[\frac{63}{32} F\left(-\frac{9}{2}, -\frac{9}{2}, 1, \left(\frac{r}{R}\right)^2\right) \left(\frac{\sigma_{sf} R}{(R^2 - r^2)}\right)^{10} - 3F\left(-\frac{3}{2}, -\frac{3}{2}, 1, \left(\frac{r}{R}\right)^2\right) \left(\frac{\sigma_{sf} R}{(R^2 - r^2)}\right)^4 \right] \quad (1)$$

The density of the adsorbate both in bulk and in confined space are calculated using the GCMC method. In this method, the grand thermodynamic potential of the system at fixed pressure, which is correlated to chemical potential, temperature and volume is minimized over the course of the simulation using the Metropolis algorithm. Simulation moves include: insertion/deletion (50%), center-of-mass translation (25%), and rotation about the center-of-mass (25%). The density of the system is calculated by averaging over a minimum of 2 x 10^6 steps after equilibration stage for at least 4 x 10^5 steps. For simulations in the bulk, the simulation box has a volume of (45 Å)^3. The system simulation box has dimensions of 30.5 Å x (2*R + 7.5) Å x (2*R + 7.5) Å.

Mesocanonical ensemble Gauge Cell MC method[26-27] is applied here to calculate the chemical potential of the adsorption system at different densities, in the vicinities of the capillary

condensation step. The simulation is performed in two cells of fixed volume, the system cell representing the pore (the same from GCMC simulations) and the gauge cell representing the gas phase. Simulation moves include molecule inter-box transfer (20%), center-of-mass translation (40%), and rotation about the center-of-mass (40%). Simulation results are calculated by averaging over N x 10^4 steps after being equilibrated for at least N x 10^3 steps, where N is the number of CO_2 molecules in the system at each point.

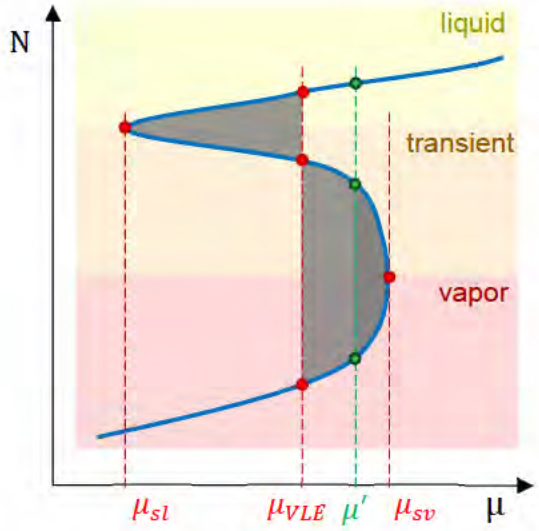

Figure 1. Canonical ensemble van-der-Waals type adsorption isotherm. The positions of vapor-liquid equilibrium and vapor and liquid spinodals are shown by red broken lines. Green broken line represents the chemical potential at which the energy barrier is being calculated.

This method provides access to metastable states by suppressing density fluctuations, allowing for the construction of the canonical ensemble isotherm in the form of the van-der-Waals loop (see Figure 1). This isotherm identifies: (i) the region, $-\infty < \mu < \mu_{sv}$, of vapor-like states, $N_v(\mu, T)$,

terminating at the vapor-like spinodal, μ_{sv}; (ii) the region, $\mu_{sl} < \mu < 0$, of liquid-like states, $N_l(\mu, T)$, terminating at the liquid-like spinodal, μ_{sl}; (iii) the backward trajectory of transient states, $\mu_{sl} < \mu < \mu_{sv}$. The transient states are unstable if the system is open; they are stabilized due to reduced fluctuations in the gauge cell method. The continuity of this isotherm allows for estimation of the equilibrium pressure and the energy barrier that separates the vapor-like and liquid-like states by thermodynamic integration. The equilibrium pressure is calculated by applying Maxwell's rule of equal areas (equation 2) to find a chemical potential, μ_{VLE}, to which the shaded area to the left is equal to the shaded area to the right. N_v, N_t, and N_l are the amount adsorbed within the vapor (v), transient (t) or liquid (l) regions.

$$\int_{\mu_{VLE}}^{\mu_{sv}} N_v(\mu)\, d\mu - \int_{\mu_{sl}}^{\mu_{sv}} N_t(\mu)\, d\mu + \int_{\mu_{sl}}^{\mu_{VLE}} N_l(\mu)\, d\mu = 0 \tag{2}$$

The energy barrier for condensation, ΔW_{vl}, is estimated by using the canonical work function, W_{CE}, which represent the work of adsorption along the canonical $N(\mu)$ isotherm,[20]

$$W_{CE}\big(N(\mu)\big) = \int_{-\infty}^{\mu} N(\mu)\, d\mu. \tag{3}$$

The work of formation of the transient state $N_t(\mu')$ from vapor state $N_v(\mu')$ is given by the difference in the respective canonical work functions,

$$\Delta W_{vl} = W_{CE}\big(N_t(\mu')\big) - W_{CE}\big(N_v(\mu')\big) = \int_{\mu'}^{\mu_{sv}} [N_t(\mu) - N_v(\mu)]\, d\mu\,, for\ \mu_{VLE} \leq \mu' < \mu_{sv}. \tag{4}$$

Here, N_t and N_v are the densities calculated from mesocanonical ensemble MC simulations for transient states and vapor states, respectively. The dotted green line in Figure 1 represents the chemical potential μ' in which the energy barrier is being calculated. As the energy barrier is proportional to the shaded area to the right of the green line, it peaks at the equilibrium chemical potential, μ_{VLE}, and diminishes at the vapor spinodal, μ_{sv}. The energy barrier E is estimated

normalizing ΔW_{vl} by the aspect ratio of the modeled pore, L* = pore length / pore diameter, to allow for comparison across systems of different size,

$$E(\mu') = \Delta W_{vl}/L^*, for\ \mu_{VLE} \leq \mu' < \mu_{sv}. \quad (5)$$

Capillary condensation should occur at equilibrium if the system is able to surpass the energy barrier E at the chemical potential μ_{VLE} of the reversible capillary condensation. Otherwise, capillary condensation should take place at a chemical potential, $\mu' > \mu_{VLE}$, at which the system can overcome the energy barrier.

Results

Experimental Adsorption Data

While analyzing the adsorption behavior, one must consider the specifics of the pore size distribution (PSD) for given material. Determined from the low temperature adsorption isotherms of N_2 and Ar (Figure 3a), the PSDs (Figure 3b) of the sample of CMK-3 considered here indicate the presence of well-defined regular primary mesopores in the range of 5-6 nm, a fraction of micropores of 0.3-0.8 nm, and a group of wider (> 7 nm) disordered secondary mesopores, as indicated by a relatively small but clearly visible shoulder. The Ar and N_2 PSD curves, obtained by using appropriate QSDFT (quenched solid density functional theory) slit-cylindrical models[43], are in perfect agreement and also in line with what has been reported previously.[39, 44]

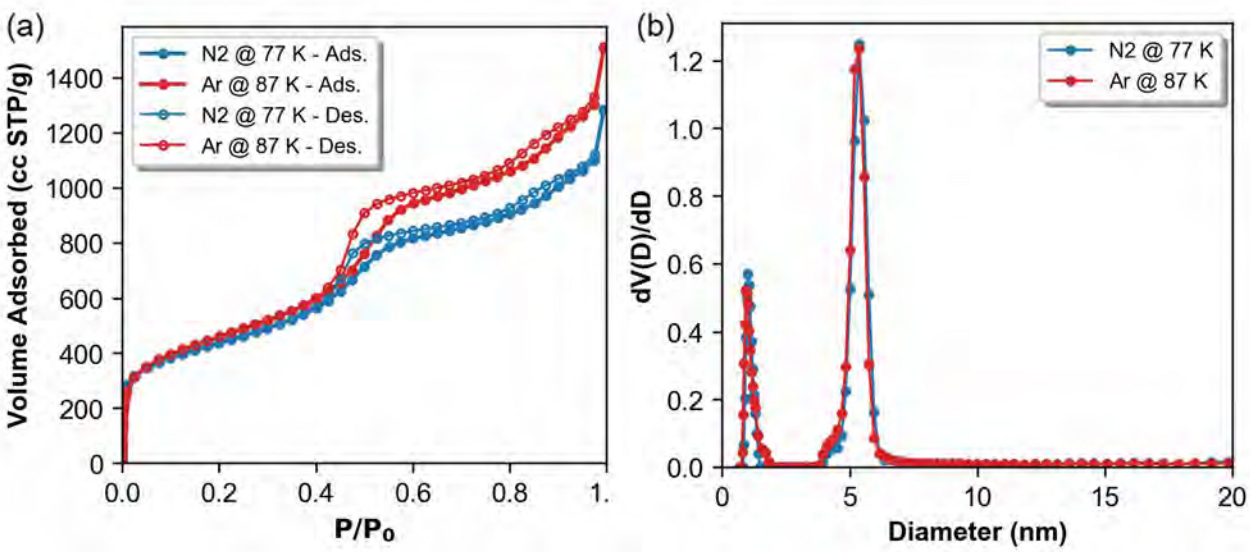

Figure 2. (a) Adsorption isotherms of N_2 (77K) and Ar (87K). (b) Pore size distribution analysis of each isotherms using QSDFT kernels.

To assess the correlation between temperature and capillary condensation regimes of CO_2 adsorption on the sample described earlier, a set of experimental measurements were performed from 185 K up to 273 K. Figure 3 shows the data in volume adsorbed (cm^3 of CO_2 per g of CMK-3) as a function of pressure in bar in a semi-log plot (Figure 3a) and relative pressure in a linear plot (Figure 3b). The semi-log plot allows for highlighting the adsorption and micropore filling region in the low-pressure range.

The isotherms at 185 and 195 K (only on Figure 3a) show the filling of micropores, but no pore filling of the mesopores could be observed although the adsorption isotherms were measured up to the corresponding saturation pressure of the solid (bulk desublimation), i.e. here it was not possible within experimental resolution to differentiate between a phase transition in the pore and in the bulk. Contrary to this, at 210 K, below the bulk triple point of CO_2 (216.6 K), the adsorption isotherm shows a clear capillary condensation with a H1-like hysteresis, same as seen in Ar (87 K) and N_2 (77 K) experiments. A similar, but narrower, hysteresis loop is observed at 220 K,

however it is absent at 240 K for the main capillary condensation step (associated with capillary condensation into the main mesopores). On the other hand, a small, yet discernible, hysteresis loop is still present at relative pressures larger than 0.7, representing capillary condensation into the secondary mesopores, indicated by the beforementioned shoulder between 6 and 10 nm in the PSD curves shown in Figure 2b.

For temperatures above 240 K, hysteresis is no longer present, as shown in the reversible isotherm at 273 K. Remarkably, observation of reversible capillary condensation over an extremely wide range of bulk-subcritical temperatures, i.e. from 304.25 K (CO_2 bulk critical temperature) down to below 240 K, indicates a significant shift of the phase diagram of CO_2 confined to mesopores. The pore critical temperature and, consequently, the hysteresis critical temperature are shifted to lower temperatures, as well as the triple point region, as indicated by the observation of capillary condensation at 210 K, ca. 6 K below the bulk triple point temperature. Qualitatively similar observations have been made for the adsorption of argon in narrow silica mesopores[45].

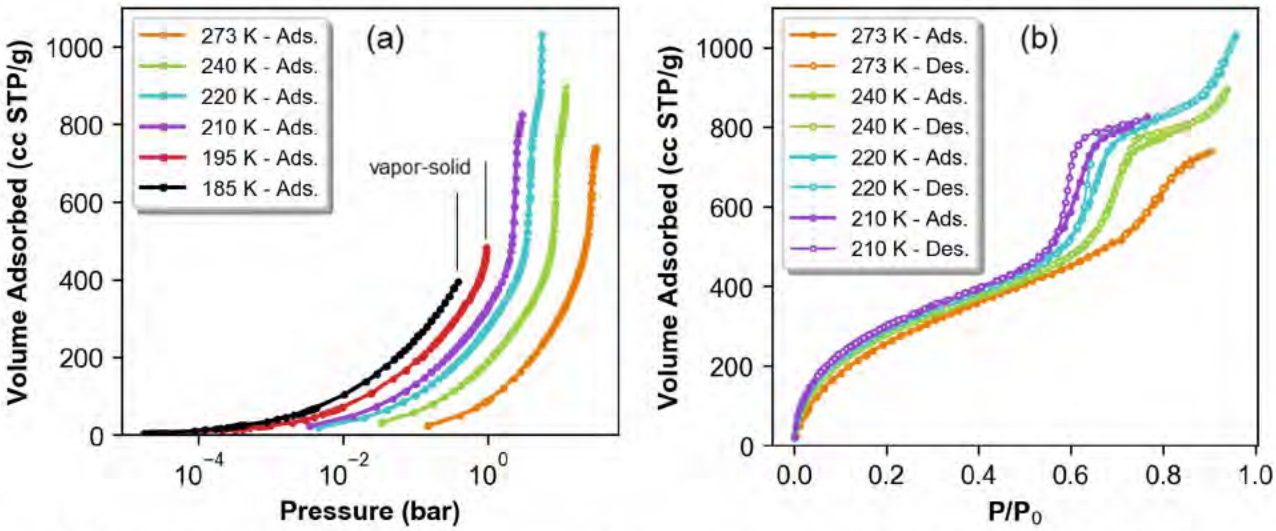

Figure 3. (a) Semi-log plot of CO_2 high-pressure adsorption isotherms in the wide range of temperatures from 185 K up to 273 K. (b) Linear plot of the adsorption isotherms from 210 K up to 273 K.

GCMC Simulations

The MC simulations were performed for a pore width of 6 nm that corresponds to the effective diameter of primary mesopores in CMK-3. In order to draw a quantitative comparison between the experimental and simulated data, the simulated isotherms in mesopores are to be augmented to account for the contribution of micropores. The theoretical isotherms presented in Figure 4 are calculated according to the following expression:

$$N(T) = V_{mi} \times \rho^{l}(T) + V_{me} \times \rho^{MC}(T) \quad (6)$$

Where the micropore volume, $V_{mi} = 0.35\ cc/g$, and the volume of primary mesopores, $V_{mi} = 1.06\ cc/g$, are estimated by minimizing the difference between the simulated and experimental data at pressures well below, and just above, the capillary condensation step. $\rho^{l}(T)$ and $\rho^{MC}(T)$, represent the bulk liquid CO_2 density and the pore fluid density calculated from MC simulations,

respectively. The quantitative relation of the isotherms for each temperature is only significant within a certain range of pressures, starting from low pressures (0.3 - 0.4 P/P_0) and up to after capillary condensation (0.65 – 0.85 P/P_0). Below this range, the micropores are not completely filled, which is reflected on the higher values of the theoretical data. Above such range, capillary condensation occurs on the secondary mesopores, leading to higher loadings than the predicted by simulations. Within the range of interest, good agreement is achieved for all temperatures with the exception of the capillary condensation step, which is predicted to occur at higher pressures than what is observed in experiments. Another aspect of comparison is the steepness of the capillary condensation step, which is more accentuated in simulations due to the ideal nature of having one pore size, rather than a pore size distribution.

Figure 4 shows the contrast between experimental adsorption isotherms (circles) and rescaled theoretical isotherms (squares) at 273, 240, 220, and 210 K. The simulated data is composed by adsorption branch, calculated using GCMC, and desorption step, defined by the equilibrium pressure calculated using the gauge cell MC method (shown by red line). While hysteresis is absent from both experiments and simulation at 273 K, it is present in the simulated data for lower temperatures. Further analysis of the comparison reveals good agreement of the equilibrium pressure from simulations compared to the inflection point of the desorption curve from the experimental data. On the other hand, the experimental condensation pressures are not reproduced by GCMC simulations, except for the highest temperature (273 K). At 240K, the simulated isotherm exhibits a prominent hysteresis, while the experimental isotherm is reversible. This observation indicates the difference in the hysteresis/pore critical temperatures in the experiments and in the simulations. This effect can be attributed to the striking difference in the observation time in real and simulated experiments and inability to cross the nucleation barrier in GCMC

simulation that occurs near the vapor spinodal. The gauge cell MC isotherms at all pressure exhibit a s-shaped van-der-Waals behavior indicating the reversible vapor-liquid equilibrium determined by the Maxwell rule. Furthermore, points near equilibrium reflect the average density at the two states (vapor-like and liquid-like), shown in more details in the Supporting Information, Section B.

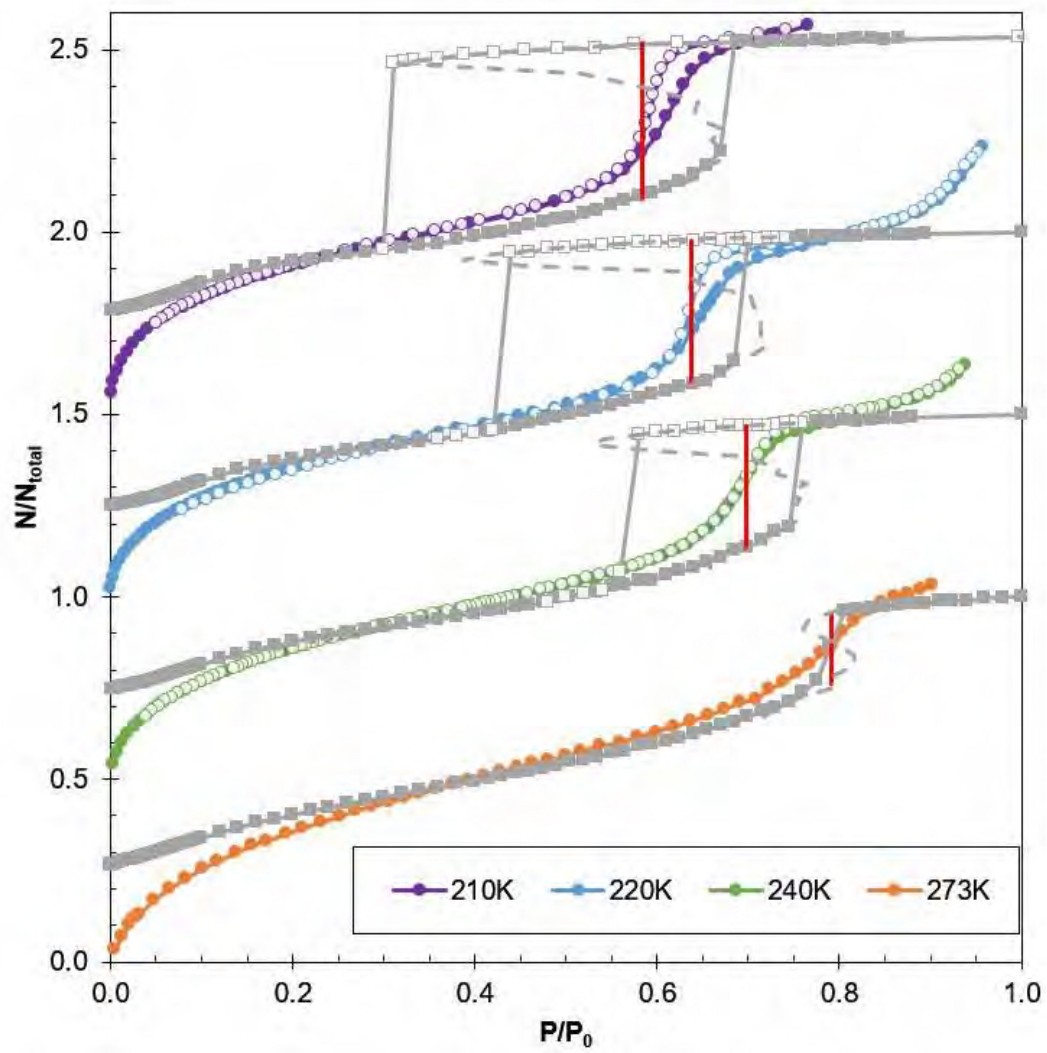

Figure 4. Comparison of experimental (circles) and GCMC simulated (squares) data at (a) 210 K, (b) 220 K, (c) 240 K and (d) 273K. The simulation data is composed by adsorption (grey closed squares), desorption (grey open squares). The canonical van-der-Waals type isotherm simulated with the gauge cell MC is shown with grey dashed line and equilibrium pressure with the red solid line. Isotherms at 240 K, 220 K, and 210 K are shifted to avoid overlap.

Condensation Pressure Estimation from Energy Barriers

To investigate the condensation pressures discrepancies between experimental and simulated data, energy barriers for each simulated gauge cell MC isotherm at pressures ranging from

equilibrium to vapor spinodal were calculated using equation 5. The results, in Figure 5, show the decrease of the energy barrier with pressure for each temperature, where the maximum is at equilibrium and approaches zero at the vapor spinodal. At 210 K, the experimental condensation pressure is about 0.62 P/P_0, the calculated energy barrier of the system at that pressure is $E_c = 43\ kT$, which is taken to be the critical energy barrier, a reference value for the experimental system. The critical energy barrier represents the maximum barrier that the real system can overcome, disregarding the temperature. Therefore, it is assumed that the condensation in experiments occurs at the pressure corresponding to the critical nucleation barrier E_c. If this pressure is larger than the equilibrium pressure, the system will exhibit hysteresis. In other words, the condensation step is delayed in the systems with the energy barrier at equilibrium larger than the critical energy barrier, $E(\mu_{VLE}) > E_c$. $E_c = 43\ kT$ determined at 210 K is used to calculate the predicted condensation pressure for other temperatures. At 210 and 220 K, the energy barrier at equilibrium is above 43 kT, thus indicating the presence of a hysteresis loop at both temperatures. Remarkable that at 240 K, when the experimental isotherm is reversible, the calculated barrier at equilibrium is around 43 kT, within the accuracy of calculation. This leads us to suggest that this temperature can be considered as the critical temperature of hysteresis of given system. At 273 K, the lack of hysteresis in both experimental and simulation data can be explained by the fact that the calculated energy barrier at equilibrium, 5 kT, is not only smaller than the critical experimental energy barrier E_c, but also smaller than the critical barrier achievable within the simulation. Such small energy barrier allows the system to jump back and forth between vapor-like and liquid-like states in the vicinity of equilibrium.

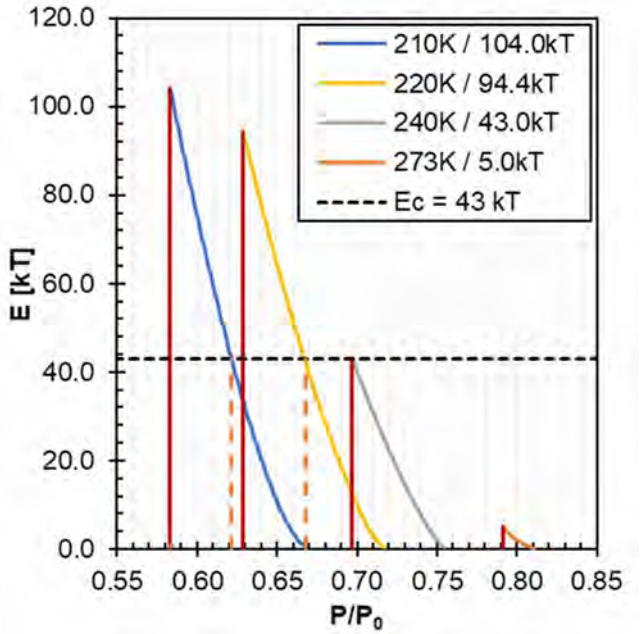

Figure 5. Energy barriers for condensation. Red solid lines indicate equilibrium conditions. Orange dotted lines represent the predicted pressures of condensation at 210 K and 220 K, at which the barrier is equal to the critical value of Ec = 43 kT.

Figure 6 further illustrates the comparison of the experimental and simulated adsorption isotherms. All isotherms are normalized by the maximum theoretical amount adsorbed in a 6 nm wide cylindrical pore.

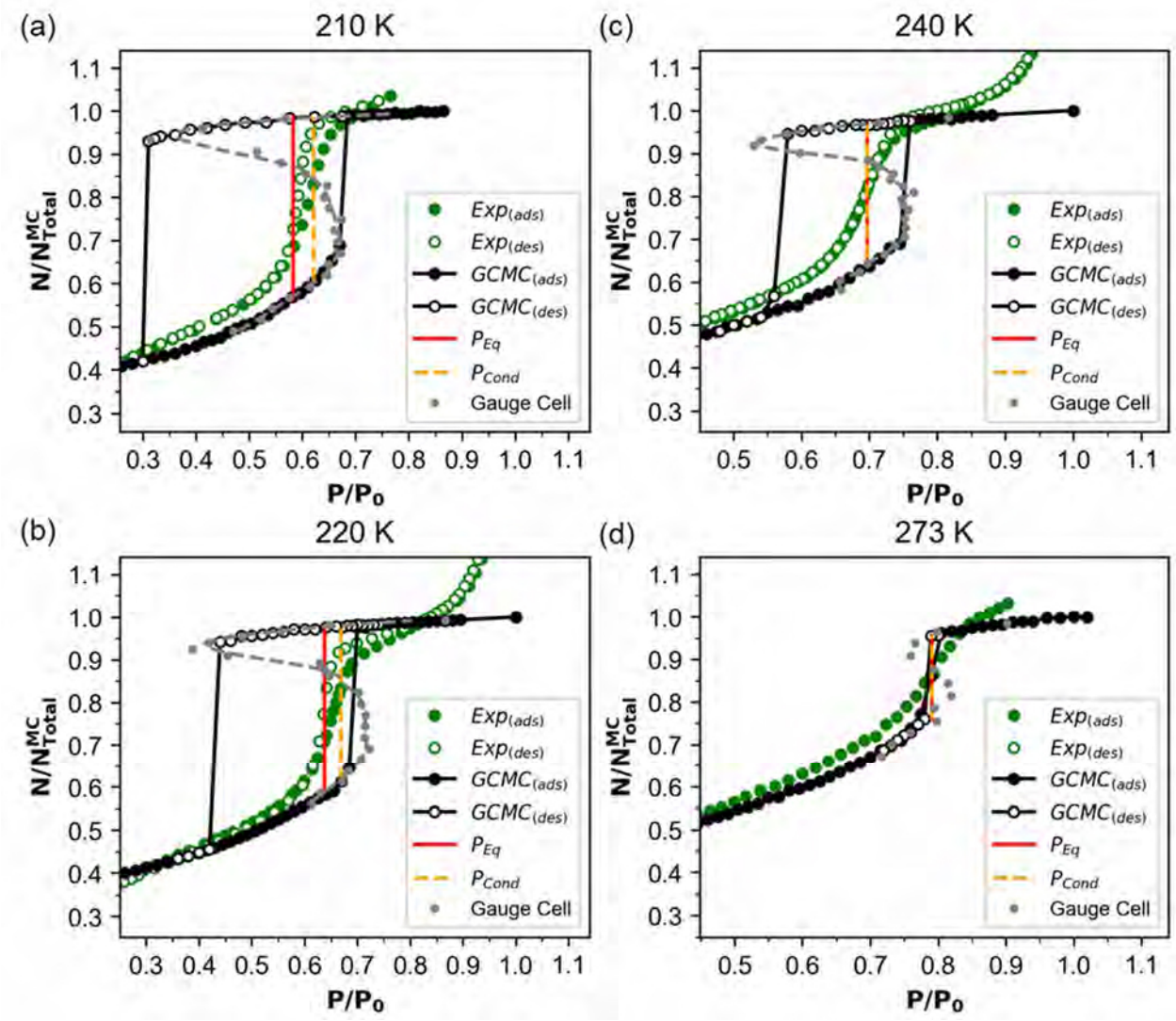

Figure 6. Comparison between experimental and simulated adsorption isotherms at (a) 210, (b) 220, (c) 240 and (d) 273 K. Both equilibrium pressures (red solid line) and estimated condensation pressures (yellow dashed line) are illustrated by vertical lines.

The snapshots displayed in Figure 7 show the final state of the simulated system at the three equilibrium characteristic points, vapor-like state (Figure 7a-d), metastable (Figure 7e-h), and liquid-like state (Figure 7i-l). Some trends can be identified from this representation, on the left column (vapor-like states), the density increases with the increase in temperature, opposite of what

is observed on the right column (liquid-like) states. Furthermore, the unstable states (middle column) display increase in density from 210 K to 240 K followed by a density decrease at 273 K.

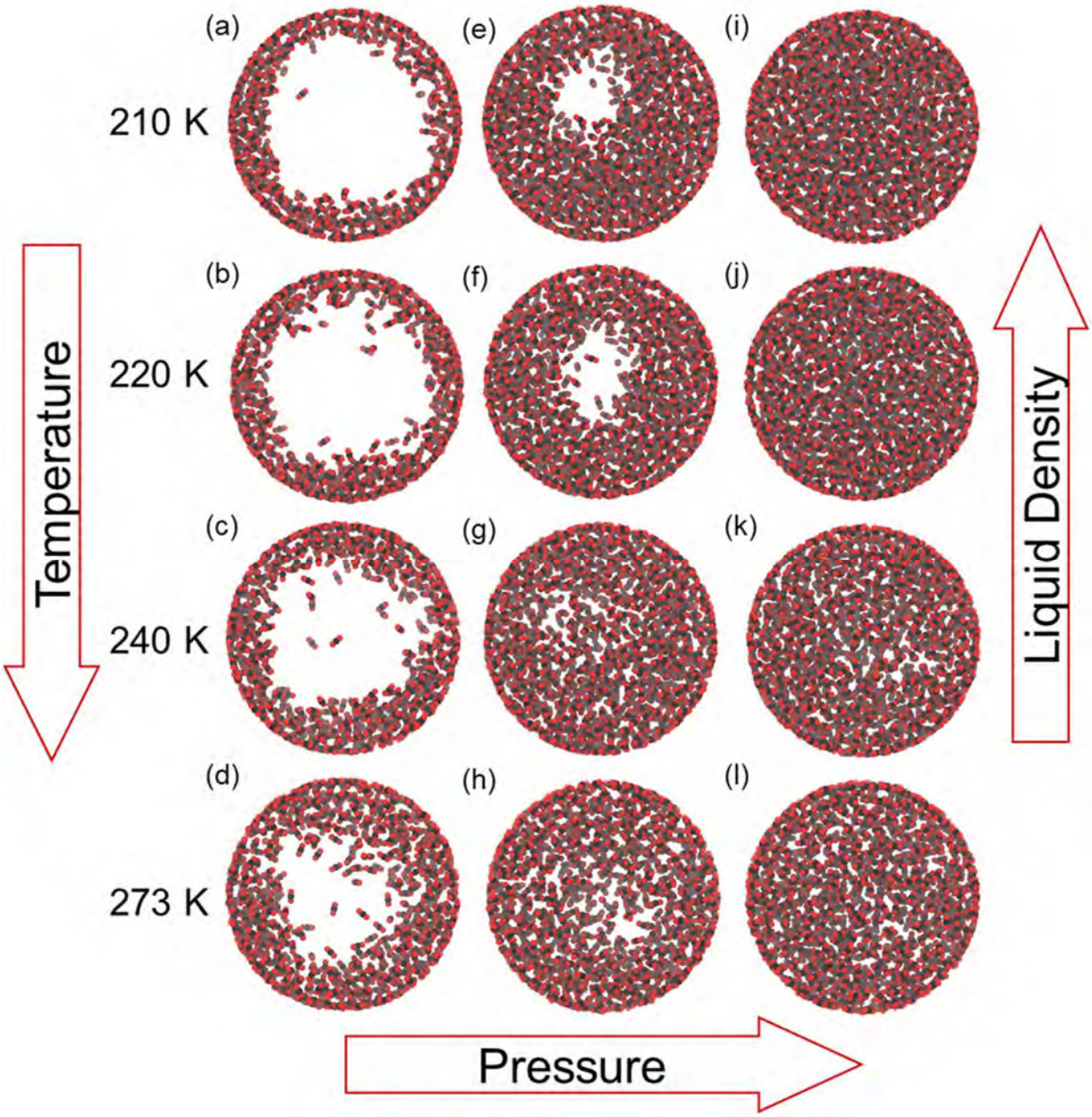

Figure 7. Snapshots of the simulated system at different temperatures showing the three different states at equilibrium pressure: (a-d) vapor-like state, (e-h) unstable state, (i-l) liquid-like state. The pore walls are not shown. CO_2 atoms are represented as spheres with oxygens in red and carbons in black.

Conclusions

A combination of the experiments and MC simulations reveals the specifics of the phase behavior of CO2 under confinement. The adsorption and desorption isotherms on a sample of CMK-3, an ordered mesoporous carbon material, are measured in the range of temperatures from 185 to 273 K. Two regimes associated with pore condensation into mesopores are found: reversible condensation at T > 240 K and capillary condensation hysteresis at 210 K < T < 240 K. The isotherms at 185 and 195 K are associated with filling of micropores only, as the adsorption isotherms were measured up to the corresponding saturation pressure of the solid (bulk desublimation); it was not possible within experimental resolution to differentiate between phase transitions in the pore and in the bulk.

The grand canonical and mesocanonical (gauge cell) simulations are performed in the model carbon cylindrical pore of 6 nm at the same temperatures as measured experimentally. To evaluate the conditions of experimentally observed hysteresis, the nucleation barriers for the condensation are estimated from the continuous gauge cell MC isotherms. Assuming that the condensation may occur provided the nucleation barrier is smaller than a certain critical energy barrier E_c, the positions of experimental condensation are calculated. $E_c = 43\,kT$ is chosen as equaled the calculated energy barrier at the experimental condensation pressure observed at 210 K. With this value, the experimentally observed hysteresis at low temperatures is fairly predicted. Moreover, it is found that at 240 K, when the experimental isotherm is reversible, the calculated barrier at equilibrium is around 43 kT. This leads us to suggest that 240 K can be considered as the critical temperature of hysteresis of given system, which separates the temperature region of equilibrium adsorption at T > 240 K and the region of developing hysteresis at T < 240 K.

With the accuracy of the predictions obtained in this work, the method developed can be used to estimate the conditions of delayed capillary condensation in pores of different sizes and at different temperatures. This allows one to determine the condensation pressures in the regime of developing hysteresis that is necessary for building the adsorption kernels for pore size distribution calculations from high pressure CO_2 adsorption data.

ASSOCIATED CONTENT

Supporting information with bulk properties and average density near equilibrium.

AKNOWLEGEMENT

This work is supported in part by the National Science Foundation (grant No 1834339)

AUTHOR INFORMATION

Corresponding Author

*aneimark@rutgers.edu, matthias.thommes@fau.de

References

1. Sun, H. Y.; Zhao, H.; Qi, N.; Li, Y., Molecular Insights into the Enhanced Shale Gas Recovery by Carbon Dioxide in Kerogen Slit Nanopores. *Journal of Physical Chemistry C* **2017,** *121* (18), 10233-10241.
2. Milner, P. J.; Siegelman, R. L.; Forse, A. C.; Gonzalez, M. I.; Runcevski, T.; Martell, J. D.; Reimer, J. A.; Long, J. R., A Diaminopropane-Appended Metal-Organic Framework Enabling Efficient CO2 Capture from Coal Flue Gas via a Mixed Adsorption Mechanism. *J Am Chem Soc* **2017,** *139* (38), 13541-13553.
3. Garrido, J.; Linaressolano, A.; Martinmartinez, J. M.; Molinasabio, M.; Rodriguezreinoso, F.; Torregrosa, R., Use of N2 Vs Co2 in the Characterization of Activated Carbons. *Langmuir* **1987,** *3* (1), 76-81.
4. Cazorla-Amorós, D.; Alcañiz-Monge, J.; Linares-Solano, A., Characterization of activated carbon fibers by CO2 adsorption. *Langmuir* **1996,** *12* (11), 2820-2824.
5. Nguyen, H. G. T.; Espinal, L.; van Zee, R. D.; Thommes, M.; Toman, B.; Hudson, M. S. L.; Mangano, E.; Brandani, S.; Broom, D. P.; Benham, M. J.; Cychosz, K.; Bertier, P.; Yang, F.; Krooss, B. M.; Siegelman, R. L.; Hakuman, M.; Nakai, K.; Ebner, A. D.; Erden, L.; Ritter, J. A.;

Moran, A.; Talu, O.; Huang, Y.; Walton, K. S.; Billemont, P.; De Weireld, G., A reference high-pressure CO2 adsorption isotherm for ammonium ZSM-5 zeolite: results of an interlaboratory study (vol 24, pg 531, 2018). *Adsorption-Journal of the International Adsorption Society* **2018,** *24* (7), 703-703.
6. Neimark, A. V.; Ravikovitch, P. I.; Vishnyakov, A., Adsorption hysteresis in nanopores. *Phys Rev E* **2000,** *62* (2 Pt A), R1493-6.
7. Thommes, M.; Kaneko, K.; Neimark, A. V.; Olivier, J. P.; Rodriguez-Reinoso, F.; Rouquerol, J.; Sing, K. S. W., Physisorption of gases, with special reference to the evaluation of surface area and pore size distribution (IUPAC Technical Report). *Pure and Applied Chemistry* **2015,** *87* (9-10), 1051-1069.
8. Cychosz, K. A.; Guillet-Nicolas, R.; Garcia-Martinez, J.; Thommes, M., Recent advances in the textural characterization of hierarchically structured nanoporous materials. *Chem Soc Rev* **2017,** *46* (2), 389-414.
9. Sing, K. S. W.; Williams, R. T., Review: The use of molecular probes for the characterization of nanoporous adsorbents. *Particle & Particle Systems Characterization* **2004,** *21* (2), 71-79.
10. De Silva, P. N. K.; Ranjith, P. G.; Choi, S. K., A study of methodologies for CO2 storage capacity estimation of coal. *Fuel* **2012,** *91* (1), 1-15.
11. Stoquart, C.; Servais, P.; Berube, P. R.; Barbeau, B., Hybrid Membrane Processes using activated carbon treatment for drinking water: A review. *J Membrane Sci* **2012,** *411*, 1-12.
12. Sun, M. H.; Huang, S. Z.; Chen, L. H.; Li, Y.; Yang, X. Y.; Yuan, Z. Y.; Su, B. L., Applications of hierarchically structured porous materials from energy storage and conversion, catalysis, photocatalysis, adsorption, separation, and sensing to biomedicine. *Chemical Society Reviews* **2016,** *45* (12), 3479-3563.
13. Zhu, K. K.; Sun, J. M.; Zhang, H.; Liu, J.; Wang, Y., Carbon as a hard template for nano material catalysts. *Journal of Natural Gas Chemistry* **2012,** *21* (3), 215-232.
14. Fan, W.; Snyder, M. A.; Kumar, S.; Lee, P. S.; Yoo, W. C.; McCormick, A. V.; Penn, R. L.; Stein, A.; Tsapatsis, M., Hierarchical nanofabrication of microporous crystals with ordered mesoporosity. *Nature Materials* **2008,** *7* (12), 984-991.
15. Jun, S.; Joo, S. H.; Ryoo, R.; Kruk, M.; Jaroniec, M.; Liu, Z.; Ohsuna, T.; Terasaki, O., Synthesis of new, nanoporous carbon with hexagonally ordered mesostructure. *J Am Chem Soc* **2000,** *122* (43), 10712-10713.
16. Zhao, D. Y.; Feng, J. L.; Huo, Q. S.; Melosh, N.; Fredrickson, G. H.; Chmelka, B. F.; Stucky, G. D., Triblock copolymer syntheses of mesoporous silica with periodic 50 to 300 angstrom pores. *Science* **1998,** *279* (5350), 548-552.
17. Thommes, M.; Findenegg, G. H., Pore Condensation and Critical-Point Shift of a Fluid in Controlled-Pore Glass. *Langmuir* **1994,** *10* (11), 4270-4277.
18. Gregg, S. J.; Sing, K. S. W., *Adsorption, surface area, and porosity*. 2nd ed.; Academic Press: London ; New York, 1982; p xi, 303 p.
19. Morishige, K.; Shikimi, M., Adsorption hysteresis and pore critical temperature in a single cylindrical pore. *J Chem Phys* **1998,** *108* (18), 7821-7824.
20. Neimark, A. V.; Vishnyakov, A., Phase transitions and criticality in small systems: vapor-liquid transition in nanoscale spherical cavities. *J Phys Chem B* **2006,** *110* (19), 9403-12.
21. Frenkel, D.; Smit, B., Chapter 5 - Monte Carlo Simulations in Various Ensembles. In *Understanding Molecular Simulation (Second Edition)*, Academic Press: San Diego, 2002; pp 111-137.

22. Wang, J. S.; Swendsen, R. H., Transition matrix Monte Carlo method. *J Stat Phys* **2002,** *106* (1-2), 245-285.
23. Berg, B. A.; Neuhaus, T., Multicanonical Ensemble - a New Approach to Simulate 1st-Order Phase-Transitions. *Phys Rev Lett* **1992,** *68* (1), 9-12.
24. Ferrenberg, A. M.; Swendsen, R. H., New Monte-Carlo Technique for Studying Phase-Transitions. *Phys Rev Lett* **1988,** *61* (23), 2635-2638.
25. Panagiotopoulos, A. Z., Direct Determination of Phase Coexistence Properties of Fluids by Monte-Carlo Simulation in a New Ensemble. *Molecular Physics* **1987,** *61* (4), 813-826.
26. Neimark, A. V.; Vishnyakov, A., Gauge cell method for simulation studies of phase transitions in confined systems. *Phys Rev E* **2000,** *62* (4 Pt A), 4611-22.
27. Neimark, A. V.; Vishnyakov, A., A simulation method for the calculation of chemical potentials in small, inhomogeneous, and dense systems. *J Chem Phys* **2005,** *122* (23), 234108.
28. Jin, B. K.; Bi, R.; Nasrabadi, H., Molecular simulation of the pore size distribution effect on phase behavior of methane confined in nanopores. *Fluid Phase Equilib.* **2017,** *452*, 94-102.
29. Jin, B. K.; Nasrabadi, H., Phase behavior of multi-component hydrocarbon systems in nano-pores using gauge-GCMC molecular simulation. *Fluid Phase Equilib.* **2016,** *425*, 324-334.
30. Hiratsuka, T.; Tanaka, H.; Miyahara, M. T., Mechanism of Kinetically Controlled Capillary Condensation in Nanopores: A Combined Experimental and Monte Carlo Approach. *ACS Nano* **2017,** *11* (1), 269-276.
31. Hiratsuka, T.; Tanaka, H.; Miyahara, M. T., Critical energy barrier for capillary condensation in mesopores: Hysteresis and reversibility. *J Chem Phys* **2016,** *144* (16), 164705.
32. Luo, S.; Lutkenhaus, J. L.; Nasrabadi, H., Confinement-Induced Supercriticality and Phase Equilibria of Hydrocarbons in Nanopores. *Langmuir* **2016,** *32* (44), 11506-11513.
33. Zeng, Y. H.; Fan, C. Y.; Do, D. D.; Nicholson, D., Condensation and Evaporation in Slit-Shaped Pores: Effects of Adsorbate Layer Structure and Temperature. *Journal of Physical Chemistry C* **2014,** *118* (6), 3172-3180.
34. Nguyen, V. T.; Do, D. D.; Nicholson, D., Reconciliation of different simulation methods in the determination of the equilibrium branch for adsorption in pores. *Molecular Simulation* **2014,** *40* (7-9), 713-720.
35. Miyahara, M. T.; Numaguchi, R.; Hiratsuka, T.; Nakai, K.; Tanaka, H., Fluids in nanospaces: molecular simulation studies to find out key mechanisms for engineering. *Adsorption-Journal of the International Adsorption Society* **2014,** *20* (2-3), 213-223.
36. Liu, Z. J.; Nguyen, V. T.; Do, D. D.; Nicholson, D., A Monte Carlo study of equilibrium transition in finite cylindrical pores. *Molecular Simulation* **2014,** *40* (12), 966-975.
37. Potoff, J. J.; Siepmann, J. I., Vapor–liquid equilibria of mixtures containing alkanes, carbon dioxide, and nitrogen. *AIChE Journal* **2001,** *47* (7), 1676-1682.
38. Huwe, H.; Froba, M., Iron(III) oxide nanoparticles within the pore system of mesoporous carbon CMK-1: intra-pore synthesis and characterization. *Microporous and Mesoporous Materials* **2003,** *60* (1-3), 151-158.
39. Thommes, M.; Morell, J.; Cychosz, K. A.; Froba, M., Combining Nitrogen, Argon, and Water Adsorption for Advanced Characterization of Ordered Mesoporous Carbons (CMKs) and Periodic Mesoporous Organosilicas (PMOs). *Langmuir* **2013,** *29* (48), 14893-14902.
40. Martin, M. G., MCCCS Towhee: a tool for Monte Carlo molecular simulation. *Molecular Simulation* **2013,** *39* (14-15), 1184-1194.
41. Tjatjopoulos, G. J.; Feke, D. L.; Mann, J. A., Molecule Micropore Interaction Potentials. *J Phys Chem-Us* **1988,** *92* (13), 4006-4007.

42. Bottani, E. J.; Bakaev, V.; Steele, W., A Simulation/Experimental Study of the Thermodynamic Properties of Carbon-Dioxide on Graphite. *Chemical Engineering Science* **1994,** *49* (17), 2931-2939.
43. Neimark, A. V.; Lin, Y. Z.; Ravikovitch, P. I.; Thommes, M., Quenched solid density functional theory and pore size analysis of micro-mesoporous carbons. *Carbon* **2009,** *47* (7), 1617-1628.
44. Gor, G. Y.; Thommes, M.; Cychosz, K. A.; Neimark, A. V., Quenched solid density functional theory method for characterization of mesoporous carbons by nitrogen adsorption. *Carbon* **2012,** *50* (4), 1583-1590.
45. Thommes, M.; Kohn, R.; Froba, M., Sorption and pore condensation behavior of pure fluids in mesoporous MCM-48 silica, MCM-41 silica, SBA-15 silica and controlled-pore glass at temperatures above and below the bulk triple point. *Applied Surface Science* **2002,** *196* (1-4), 239-249.